The Journal of Experimental Biology 212, 2436-2447
Published by The Company of Biologists 2009
doi:10.1242/jeb.026740

Flow structures and fluid transport for the hydromedusae *Sarsia tubulosa* and *Aequorea victoria*

Doug Lipinski and Kamran Mohseni*
College of Engineering and Applied Science, University of Colorado at Boulder, Boulder, CO 80309, USA
*Author for correspondence (e-mail: mohseni@colorado.edu)

Accepted 8 May 2009 (submitted 27 October 2008)

SUMMARY

The flow structures produced by the hydromedusae *Sarsia tubulosa* and *Aequorea victoria* are examined using direct numerical simulation and Lagrangian coherent structures (LCS). Body motion of each hydromedusa is digitized and input to a CFD program. *Sarsia tubulosa* uses a jetting type of propulsion, emitting a single, strong, fast-moving vortex ring during each swimming cycle while a secondary vortex of opposite rotation remains trapped within the subumbrellar region. The ejected vortex is highly energetic and moves away from the hydromedusa very rapidly. Conversely, *A. victoria*, a paddling type hydromedusa, is found to draw fluid from the upper bell surface and eject this fluid in pairs of counter-rotating, slow-moving vortices near the bell margins. Unlike *S. tubulosa*, both vortices are ejected during the swimming cycle of *A. victoria* and linger in the tentacle region. In fact, we find that *A. victoria* and *S. tubulosa* swim with Strouhal numbers of 1.1 and 0.1, respectively. This means that vortices produced by *A. victoria* remain in the tentacle region roughly 10 times as long as those produced by *S. tubulosa*, which presents an excellent feeding opportunity during swimming for *A. victoria*. Finally, we examine the pressure on the interior bell surface of both hydromedusae and the velocity profile in the wake. We find that *S. tubulosa* produces very uniform pressure on the interior of the bell as well as a very uniform jet velocity across the velar opening. This type of swimming can be well approximated by a slug model, but *A. victoria* creates more complicated pressure and velocity profiles. We are also able to estimate the power output of *S. tubulosa* and find good agreement with other hydromedusan power outputs. All results are based on numerical simulations of the swimming jellyfish.

Supplementary material available online at http://jeb.biologists.org/cgi/content/full/212/15/2436/DC1

Key words: hydromedusae, feeding, jet propulsion, rowing propulsion, Lagrangian coherent structures, LCS.

INTRODUCTION

Two distinct types of hydromedusan propulsion are well known (Colin and Costello, 2002). Prolate species such as *Sarsia tubulosa* primarily use a jetting type of propulsion with large jet velocities immediately behind the velar aperture. Their swimming is characterized by quick accelerations during the contraction phase of swimming followed by periods of gliding with relatively small accelerations. However, the once widely accepted jetting model fails to explain the swimming patterns seen in prolate species such as *Aequorea victoria*. These hydromedusae use a paddling or rowing motion to swim and produce more diffuse vortices shed from the bell margins during the contraction phase.

Prolate, jetting hydromedusae retract their tentacles during swimming and feed by extending their tentacles while drifting (Madin, 1988). Swimming is used to escape predators or to ambush prey. Swimming and feeding are disparate activities since extending the tentacles during swimming could greatly decrease swimming performance. Conversely, oblate, paddling hydromedusae leave their tentacles extended during swimming and the vortices produced during swimming travel through the extended tentacles (Colin and Costello, 2002; Colin et al., 2003; Costello, 1992; Costello and Colin, 1994; Ford and Costello, 1997). Prey in the fluid near the bell region of paddling hydromedusae have even been observed to be carried into contact with the tentacles by the vortices formed during swimming (Costello and Colin, 1995). For these reasons, swimming complements feeding in paddling hydromedusae by helping to draw prey into the tentacles.

It has been shown that rowing propulsion is a necessary adaptation for larger hydromedusae due to morphological constraints and energy efficiency. For jetting propulsion, the force necessary for propulsion increases faster with size than the available muscle force to provide the jetting motion (Dabiri et al., 2007). Oblate hydromedusae make up for this by employing paddling type propulsion. Models show that the production of stopping vortices during the relaxation phase of paddling type propulsion allows large hydromedusae to swim effectively despite their morphological constraints (Dabiri et al., 2007). Specifically, the stopping vortex partially cancels the starting vortex, reducing the induced drag on the oblate hydromedusa and increasing swimming efficiency. The smaller, prolate species have lower drag due to their shape and further decrease drag by retracting their tentacles while swimming (Colin et al., 2003). These factors, combined with more rapid bell contractions, make jetting hydromedusae much more proficient swimmers than their oblate relatives (Daniel, 1983).

We are interested in hydromedusan propulsion as a basis for the design of new propulsion technologies for underwater vehicles. Recently, jet and vortex propulsion have become a focus in the areas of underwater maneuvering and locomotion of bio-engineered vehicles. A vortex thruster loosely mimicking hydromedusa propulsion was proposed by Mohseni (Mohseni, 2004; Mohseni, 2006). The current generation of these thrusters and their implementation on an underwater vehicle are discussed by Krieg and Mohseni (Krieg and Mohseni, 2008) and are capable of

producing very strong vortices (formation time of up to 15, see Results for a discussion of formation numbers). Mohseni et al. (Mohseni et al., 2001) and Dabiri and Gharib (Dabiri and Gharib, 2005) also reported numerical and experimental results for jets formed from a nozzle with temporally varying exit velocity and diameter, respectively.

In the present study, we present the Lagrangian coherent structures (LCS) seen in the results of numerical simulations of hydromedusae swimming as well as several examples of particle motion in the resulting flow. The hydromedusae examined are *Aequorea victoria* Murbach and Shearer 1902, a paddling or rowing type of hydromedusa, and *Sarsia tubulosa* M. Sars 1835, a jetting type of hydromedusa. We believe this to be the first numerical study of this type. The actual motion of the hydromedusa, reproduced from digitized videos of the swimming hydromedusae, is used to compute the surrounding velocity field. A brief description of the numerical method for computing the velocity field is included in Materials and methods. The use of computational fluid dynamics (CFD) data instead of an empirical velocity field from digital particle image velocimetry (DPIV), or similar, results in higher resolution of the LCS as well as greater accuracy in subsequent calculations. Additionally, there are significant difficulties in obtaining high-quality results from DPIV for swimming hydromedusae. DPIV results are only available for the time during which the hydromedusa is properly oriented within the field of view, perhaps only a few swimming cycles depending on many factors. Additionally, the resolution obtained from DPIV depends on the concentration of particles in a given region. In general, the distribution of particles may be highly non-uniform. The particles will be drawn toward certain flow structures, just as dye is drawn into vortices in dye visualization experiments, but other areas of the flow may be left with few particles. None of these difficulties are present in our method. It is only necessary to capture a good swimming cycle. The periodic swimming motion may then be determined up to the resolution of the camera used and iterated for as many swimming cycles as desired.

As expected, *S. tubulosa* produces strong vortices along the axis of symmetry. These vortices move quickly away from the hydromedusa, providing a high momentum transfer for rapid swimming while negating opportunities for feeding while swimming. In fact, if *S. tubulosa* were to extend its tentacles during swimming, they would create additional drag and could negatively impact swimming performance. Conversely, the structures formed by the paddling hydromedusa, *A. victoria*, transport fluid from the outer bell surface to linger in the tentacle region, enhancing feeding opportunities since the flow passes through the region where the tentacles drift.

We also note the presence of previously unobserved flow structures in the subumbrellar region of *S. tubulosa*. As previously mentioned, *A. victoria* produces a starting and stopping vortex during each swimming cycle. Since these vortices are ejected together during the contraction phase, they interact and influence each other. We find that *S. tubulosa* also produces a stopping vortex during the relaxation phase. However, only the starting vortex is ejected during contraction while the stopping vortex mostly dissipates within the subumbrellar cavity. Finally, we examine the pressure on the subumbrellar wall of both hydromedusae as well as the velocity profiles in the wake and across the velar opening. *Sarsia tubulosa* produces a nearly uniform jet through the velar opening and an equally uniform pressure along the subumbrellar wall. We expect that this type of swimming could be very well approximated by a slug model or a piston-cylinder arrangement. Conversely, *A. victoria* produces a much more complicated wake and pressure profile.

MATERIALS AND METHODS

Hydromedusa motion

The motion of each hydromedusa was determined from videos of physical specimens of the swimming hydromedusae. These videos were provided by Dr Sean Colin (Roger Williams University) and are further discussed in Sahin et al. (Sahin et al., 2009). The hydromedusae were placed in filtered seawater within a glass vessel of sufficient size to allow each hydromedusa to swim freely. The outline of the bell was illuminated using a planar laser directed through the central axis. Fluorescein dye was injected near the bell to enhance the illumination.

After recording, each frame of the video was analyzed, and the body motion of the hydromedusa was determined. The geometry of the hydromedusa was approximated using NURBS curves (Piegl, 1991), and Fourier-series interpolation in time was used to create a numerical model of the periodic contraction of the swimming hydromedusae. In contrast to the relatively short time frames allowed by using DPIV, this model allows us to analyze many periods of swimming *via* numerical solution for the flow around the hydromedusa.

Numerical procedure

For completeness, a brief overview of the numerical procedure used in the computation of the velocity field induced by the swimming hydromedusae is included here. For complete details of the numerical procedure we have developed for this problem, including code validation, see Sahin and Mohseni (Sahin and Mohseni, 2008a; Sahin and Mohseni, 2008b). The flow field was computed based on the periodic swimming model derived from the videos of swimming hydromedusae. The surrounding velocity field was computed using a new arbitrary Lagrangian–Eulerian (ALE) (Hirt et al., 1974) method developed for this purpose. In this method, the mesh follows the moving boundary between the fluid and the hydromedusa body, and the cylindrically symmetric governing equations are solved on a moving, unstructured quadrilateral mesh. The pressure is solved on a staggered grid, eliminating the need for pressure boundary conditions since pressure is defined only at interior points. The mesh motion is determined by solving the linear elasticity equation at each time to avoid remeshing (Dwight, 2006; Johnson and Tezduyar, 1994), and the linear systems produced by the discretization are solved using the GMRES method (Saad and Schultz, 1986) combined with several preconditioners.

Lagrangian coherent structures

Lagrangian coherent structures provide a method of analyzing a flow field from a dynamical systems perspective. LCS were introduced by Haller and Yuan (Haller and Yuan, 2000) and further defined by Shadden et al. (Shadden et al., 2005). LCS represent lines of negligible fluid flux in a flow and therefore govern transport and mixing in the flow. Due to the general framework provided by LCS, they have been applied to a wide range of different areas including transport of pollutants in the ocean (Lekien et al., 2005), two-dimensional turbulence (Haller and Yuan, 2000; Manikandan et al., 2007), vortex shedding behind an airfoil (Cardwell and Mohseni, 2008; Lipinski et al., 2008) and transport in empirical vortex rings as well as hydromedusa swimming (Shadden et al., 2006). LCS have proven to be an effective tool for identifying exact vortex boundaries and can even be used to divide a flow into lobes that govern transport, as is done in classical lobe dynamics analysis (Rom-Kedar and Wiggins, 1990). We follow the procedure for computing LCS outlined by

Shadden et al. (Shadden et al., 2005) and we provide here a brief overview for those unfamiliar with this concept.

It is simplest to think of LCS as a post-processing technique to reveal coherent structures in a given flow. In our case, the flow is determined by numerical simulations of the swimming hydromedusae. LCS are based on the finite time Lyapunov exponent (FTLE), which is analogous to the standard Lyapunov exponent of classical dynamical systems theory. The FTLE is defined as:

$$\sigma_{t_0}^{T}(\mathbf{x}) = \frac{1}{|T|}\ln\sqrt{\lambda_{\max}(\Delta)}\,, \tag{1}$$

where t_0 is the time being considered, T is the 'integration time', which will be further explained later, $\mathbf{x}$ is the position vector, and $\lambda_{\max}(\Delta)$ is the maximum eigenvalue of the finite time deformation tensor, Δ. In practice, the domain of interest is seeded with passive tracer particles, which are then advected from time t_0 to time t_0+T using the known velocity field. The resulting particle positions are then used to compute Δ and then the FTLE field. The flow considered here is a two-dimensional, axisymmetric flow, and Δ was calculated appropriately to take this into account. In swirl-free axisymmetric coordinates, (r, θ, x), Δ becomes:

$$\Delta = \left(\frac{\mathrm{d}\Phi}{\mathrm{d}\mathbf{x}}\right)^{*}\left(\frac{\mathrm{d}\Phi}{\mathrm{d}\mathbf{x}}\right), \tag{2}$$

$$\frac{\mathrm{d}\Phi}{\mathrm{d}x} = \begin{pmatrix} \frac{\partial r_\mathrm{f}}{\partial r_\mathrm{i}} & 0 & \frac{\partial r_\mathrm{f}}{\partial x_\mathrm{i}} \\ 0 & \frac{r_\mathrm{f}}{r_\mathrm{i}} & 0 \\ \frac{\partial x_\mathrm{f}}{\partial r_\mathrm{i}} & 0 & \frac{\partial x_\mathrm{f}}{\partial x_\mathrm{i}} \end{pmatrix}, \tag{3}$$

where r_i, r_f, x_i and x_f are the initial and final radial and axial coordinates of a particle in the flow, respectively.

The resulting FTLE field depends on the integration time, T, in that larger values of T reveal more structures than smaller values of T. Therefore, T may be chosen to reveal the desired level of detail without worrying about influencing the major structures that are revealed. Additionally, T may be positive or negative, representing forward and backward particle advection, respectively. Therefore, there are two types of FTLE fields: forward time and backward time.

Once the FTLE field has been calculated, LCS are defined as ridges in the FTLE field, following Shadden et al. (Shadden et al., 2005). In practice, LCS are usually visualized by looking at contour plots of the FTLE field. Conceptually, ridges in the forward FTLE field, called forward LCS, represent lines where particles diverge most quickly, and backward LCS represent lines where particles converge. For this region, dye visualization experiments reveal structures very similar to backward LCS. Additionally, for LCS which are sufficiently strong, the flux across the LCS is negligible, a property that makes LCS extremely useful for analyzing transport in flows. Finally, forward LCS are analogous to the stable manifolds of a dynamical system and act as repelling material lines while backward LCS are analogous to the unstable manifolds of a dynamical system and act as attracting material lines. The interaction of these LCS largely govern transport in a flow, and their intersections can be used to exactly define a vortex without the use of arbitrary thresholds of vorticity (Shadden et al., 2006).

RESULTS

Sarsia tubulosa

Sarsia tubulosa employs a jetting type of propulsion. The swimming cycle consists of three phases: (1) a rapid contraction, (2) relaxation and (3) a coasting phase. Each cycle results in the expulsion of a strong vortex along the axis of symmetry, which rapidly propels the jellyfish forward as seen in the LCS shown in Fig. 1 (also see Movie 1 in supplementary material).

The jetting nature of *S. tubulosa*'s propulsion, forming a single vortex ring with each swimming pulse, is clearly reflected in the LCS seen in Fig. 1. During the contraction phase, a vortex which draws fluid in the positive x-direction along the axis of symmetry is ejected from the hydromedusa. This will be referred to as the starting vortex. One of the most striking details of this figure is the presence of very complex flow structures within the subumbrellar

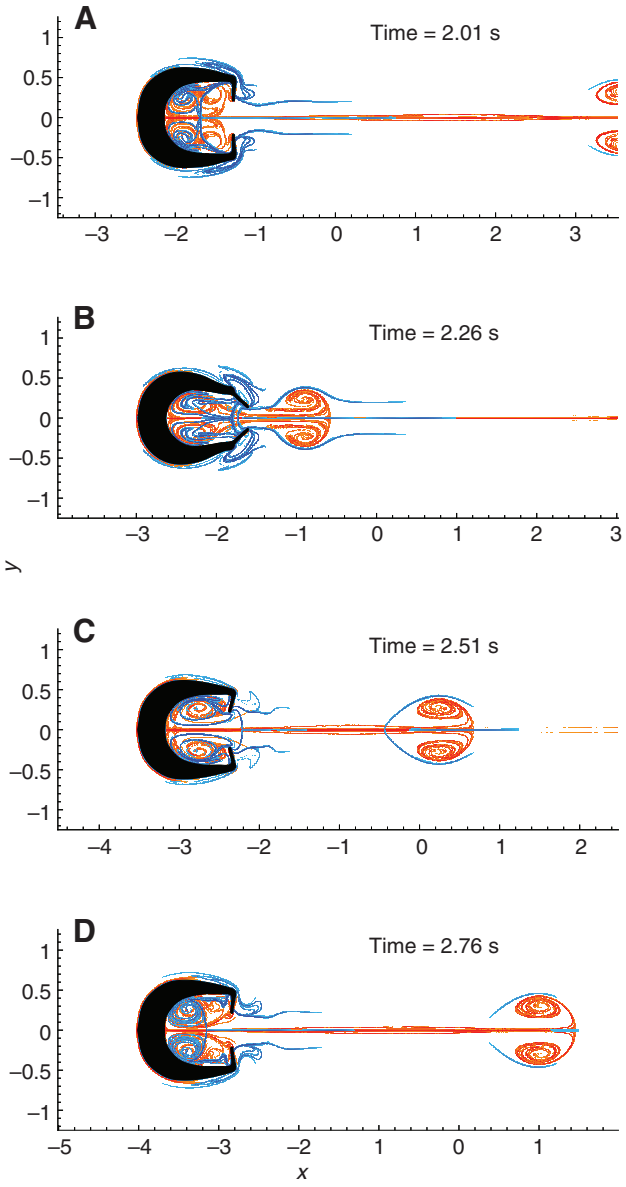

Fig. 1. Lagrangian coherent structures (LCS) for one swimming cycle of *Sarsia tubulosa*. The forward LCS are shown in blue and the backward LCS are red. The video version is available in the supplementary material as Movie 1.

region of the jetting hydromedusa. This region is very difficult to view experimentally with DPIV or other techniques. However, our numerical technique shows that during the relaxation phase of swimming (Fig. 1C), a stopping vortex of opposite sense to the ejected vortex forms within the subumbrellar cavity. In this hydromedusa, the presence of the velum traps the stopping vortex within the subumbrellar cavity. Since the stopping vortex is not ejected, it cannot interact with the ejected starting vortex. This is the first time this stopping vortex has been observed in jetting hydromedusae, likely due to the difficulty in imaging the subumbrellar cavity of jetting hydromedusae during experiments. In fact, it has been recently stated that no stopping vortex is formed in a jetting swimmer (Weston et al., 2009), but we suspect this vortex is present, even if difficult to detect, in all jetting as well as paddling hydromedusae.

Our simulations for *S. tubulosa* used a hydromedusa with a maximum bell radius of 0.63 cm, a minimum bell radius of 0.57 cm and a swimming cycle length of 1 s with 100 time steps per cycle. In addition, the subumbrellar volume had a maximum value of approximately 0.45 cm^3 and a minimum value of 0.26 cm^3.

Sarsia tubulosa is very efficient at producing a strong vortex. We can quantify this ability by examining the formation time of the vortices produced. Gharib et al. (Gharib et al., 1998) defined the dimensionless formation time as:

$$T^* = \frac{\overline{U_e}t}{D_e}\,, \tag{4}$$

for a jet of velocity U_e through a nozzle of constant diameter D_e over a time t where the bar denotes a running mean. However, for a non-constant exit diameter it is necessary to consider an integral form of this equation. Calculations for a slug of fluid ejected from an orifice with time varying diameter and velocity were presented by Mohseni (Mohseni, 2000). Using a similar approach, Dabiri and Gharib (Dabiri and Gharib, 2005) derived:

$$T^* = \int_0^t \frac{U_e(\tau)}{D_e(\tau)}\,d\tau\,. \tag{5}$$

In the case of constant density flow, such as a hydromedusa swimming in water, conservation of mass allows us to express this as:

$$T^* = \int_0^t \frac{U_e(\tau)}{D_e(\tau)}\,d\tau = -\frac{\pi}{4}\int_0^t D_e(\tau)\frac{dV_e(\tau)}{d\tau}\,d\tau\,, \tag{6}$$

where V_c is the volume of the cavity; in our case, the subumbrellar volume.

A larger formation time indicates the formation of a more effective vortex, where an impulsively started piston-cylinder arrangement produces a formation time of about 4, after which additional fluid expulsion results in a trailing jet behind the vortex (Gharib et al., 1998). *Sarsia tubulosa* produces a vortex with a formation time $T^* \approx 7$. This large formation number was expected, as discussed by Dabiri et al. (Dabiri et al., 2006), and is made possible largely by the decrease in diameter of the velar opening during the contraction phase of swimming (see Fig. 2). A trailing jet represents a decreased efficiency of momentum and energy transfer (Krueger and Gharib, 2003). The vortex ring produced by *S. tubulosa* has no such trailing jet, meaning the vortices are formed with maximal efficiency.

The axial velocity in the wake is plotted in Fig. 3. This plot represents one swimming cycle and clearly shows that the velocity disturbances are concentrated near the axis of symmetry. In fact, beyond about one-half a diameter away from the axis of symmetry, the disturbances quickly decay to negligible levels. As a vortex is produced, a large axial velocity appears at the velar opening of the hydromedusa, which then decays as the vortex moves away from the hydromedusa. Also, the velocity in the wake is almost entirely positive due to the jetting nature of the swimming. The strong jet can also be seen in the plot of axial velocity across the velar opening as well as the pressure on the subumbrellar wall (Fig. 4 and Fig. 5). Notice, in particular, that the velocity across the velar opening forms a very uniform jet, with only a small shear layer near the velum. This is in contrast to the profile that we will see for *A. victoria*. Additionally, we can divide the swimming cycle for *S. tubulosa* into three parts: a strong contraction, a relaxation phase and then a brief coasting phase before the next contraction. These three phases can be clearly seen as a decrease, then increase, in the subumbrellar volume followed by a time of nearly constant volume as seen in Fig. 2.

By noting that *S. tubulosa* is a jetting swimmer, propelling itself *via* a jet created by pressurizing the subumbrellar cavity, we can calculate the power output similarly to a biological (such as a heart) or mechanical pump, as has been done for squids (O'Dor, 1988). The power output is simply given by $P_{out} = p\dot{Q}$, where p is the subumbrellar pressure and $\dot{Q}$ is the jet flow rate. Since the pressure and jet velocity are very uniform in space (see Figs 4 and 5), we can use the mean value at each time step without losing much accuracy. $\dot{Q}$, p and P_{out} are plotted in Fig. 6.

The mean power output is found to be about 16 $g\,cm^2\,s^{-3}$. To account for body size, power is divided by mass to the 5/3 power (see Daniel, 1983), where this *S. tubulosa* has a mass of ~0.65 g as calculated from the volume of the body and the assumption of neutral buoyancy (1 $g\,cm^{-3}$). This results in a mean power output of ~0.33 $W\,kg^{-5/3}$, which is within the reported range

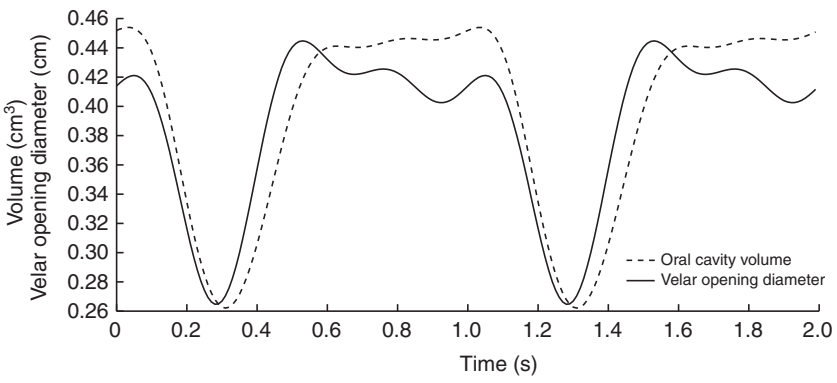

Fig. 2. The subumbrellar volume and velar opening diameter during two swimming cycles for *Sarsia tubulosa*.

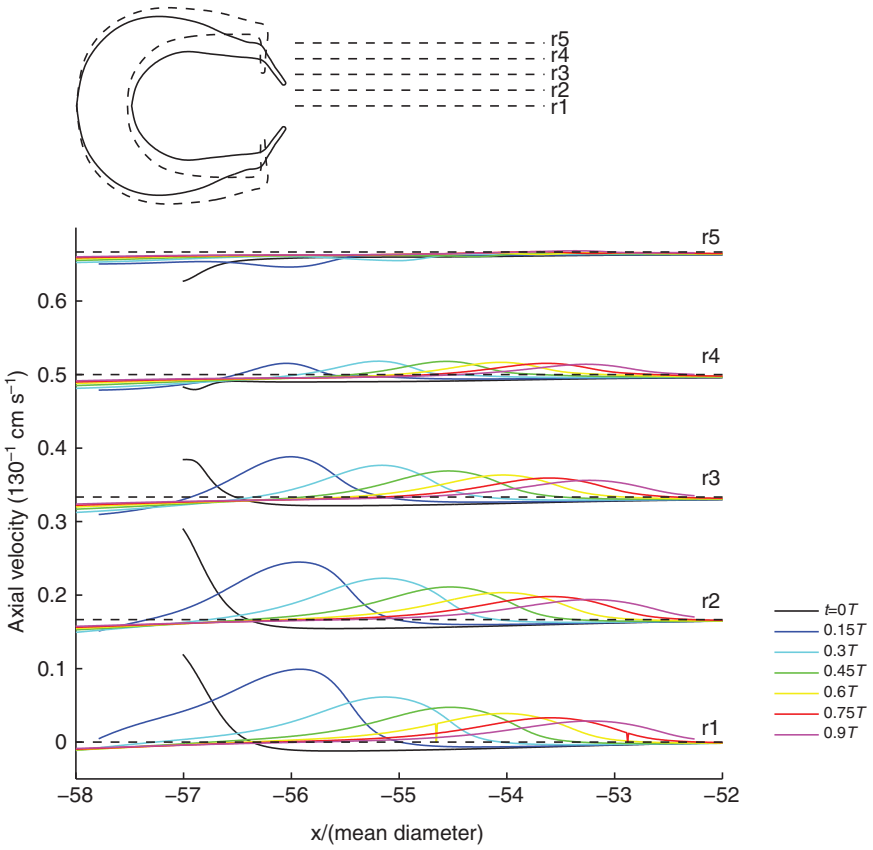

Fig. 3. The axial velocity along lines of constant radius in the wake of *Sarsia tubulosa*. The radii chosen, along with the hydromedusa geometry at minimum and maximum diameter, are shown. The radius has been scaled by the mean diameter and the velocity has been scaled by a factor of 130^{-1} to fit within the figure. Many times, from t=0T to 0.9T (T=1 s=one paddling cycle), representing one paddling cycle are plotted, with darker lines representing the most recent times.

(0.2–0.75 W kg$^{-5/3}$) of the experimentally measured power outputs for the hydromedusae *Gonionemus vertens* and *Stomotoca atra* (Daniel, 1985).

Since there is only negligible flux across LCS, they largely govern transport in a given flow (Shadden et al., 2005). In fact, the intersections of forward and backward LCS divide the flow into lobes that have distinct mixing characteristics. It is interesting to ask where the particles in a vortex come from. Figs 7–9 show the motion of passive tracers for the swimming *S. tubulosa* (also see Movie 2 in supplementary material). In this jetting hydromedusa, the LCS are complicated and evolve very quickly during the contraction phase so that the groups of tracers that end up in a vortex are not clearly separated upstream of the hydromedusa (Fig. 7A). As the hydromedusa swims, the green group of tracers is pulled into the subumbrellar cavity while the blue and red groups collect outside the bell (see Fig. 8B). Then, just before the contraction phase, the

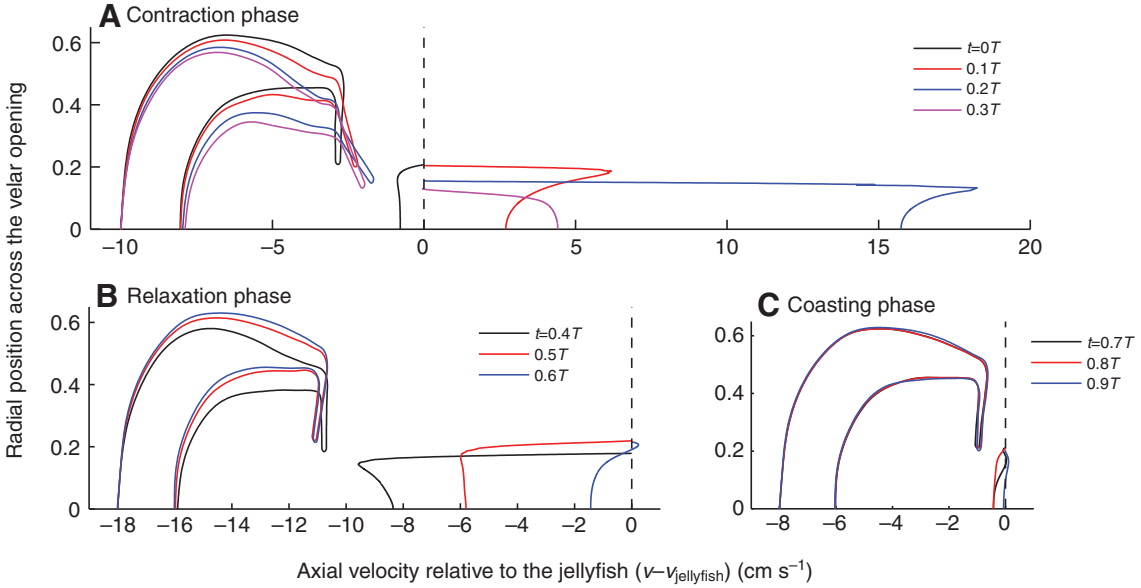

Fig. 4. The axial velocity of the flow relative to the hydromedusa across the velar opening of *Sarsia tubulosa*. Times are presented for one complete paddling cycle.

blue group is pulled into the subumbrellar cavity while the red group remains outside (Fig. 9A). The red and blue groups of tracers merge and are ejected with the vortex ring, at which point the dark red group of tracers begins to be wrapped into the vortex ring as well (Fig. 9B,C). The ejected drifters travel away from the hydromedusa very quickly as they are carried with the traveling vortex ring.

The best way to quantify this is to define the Strouhal number as $St=fL/v$, where f is frequency, L is the mean hydromedusa radius and v is the rate of vortex separation from the hydromedusa. *Sarsia tubulosa* has a Strouhal number of about 0.10, meaning that the vortices separate from the hydromedusa by about 10 radii per swimming cycle. As we will discuss in more detail later, this presents little opportunity for feeding during swimming.

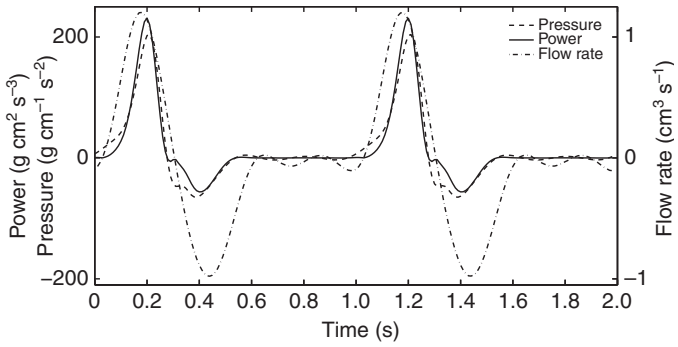

Fig. 6. The power output (P_{out}), pressure (p) and flow rate ($\dot{Q}$) during two swimming cycles for *Sarsia tubulosa*.

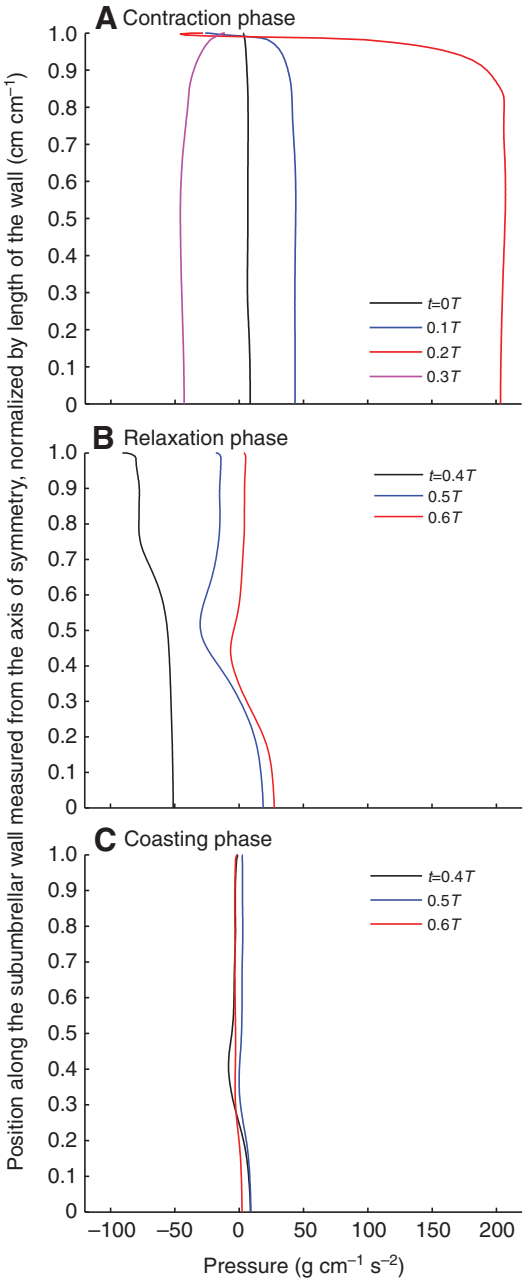

Fig. 5. The pressure on the subumbrellar wall of *Sarsia tubulosa* for one swimming cycle. The position is normalized by the length of the subumbrellar wall and pressure is given in g cm^{-1} s^{-2}.

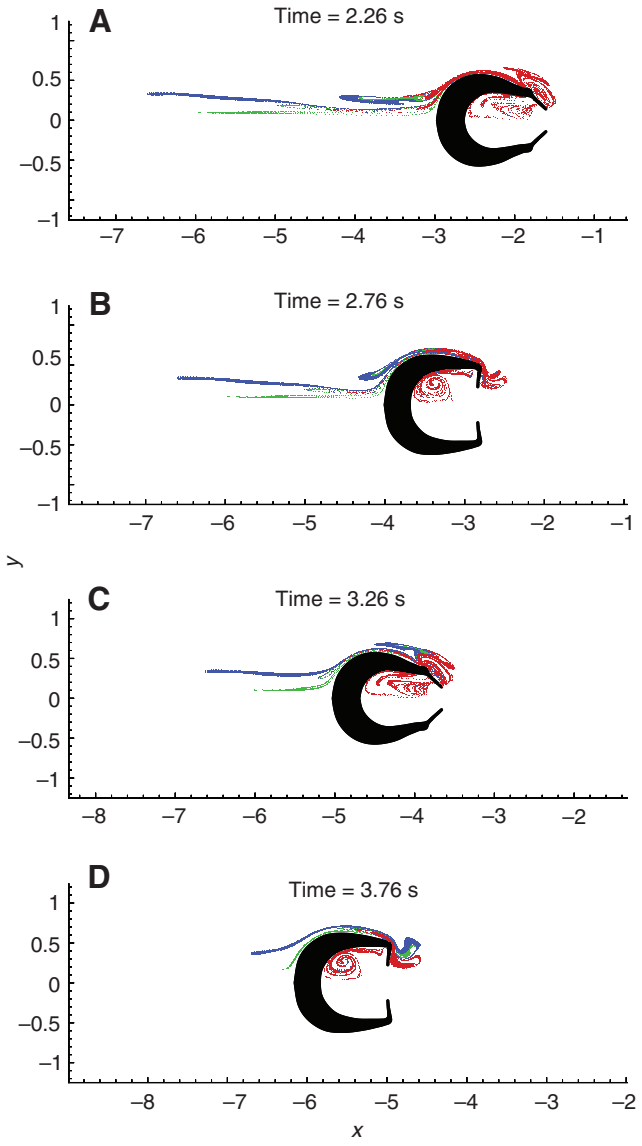

Fig. 7. Passive tracer particles for *Sarsia tubulosa*. There are three groups of tracer particles, colored green, blue and red, which are ejected as part of the same vortex. See Movie 2 in supplementary material.

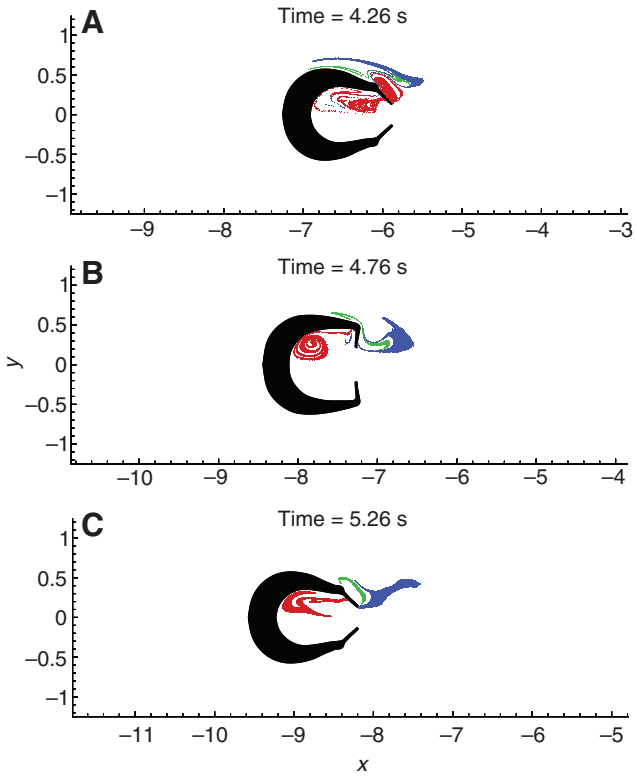

Fig. 8. Passive tracer particles for *Sarsia tubulosa*. There are three groups of tracer particles, colored green, blue and red, which are ejected as part of the same vortex. See Movie 2 in supplementary material.

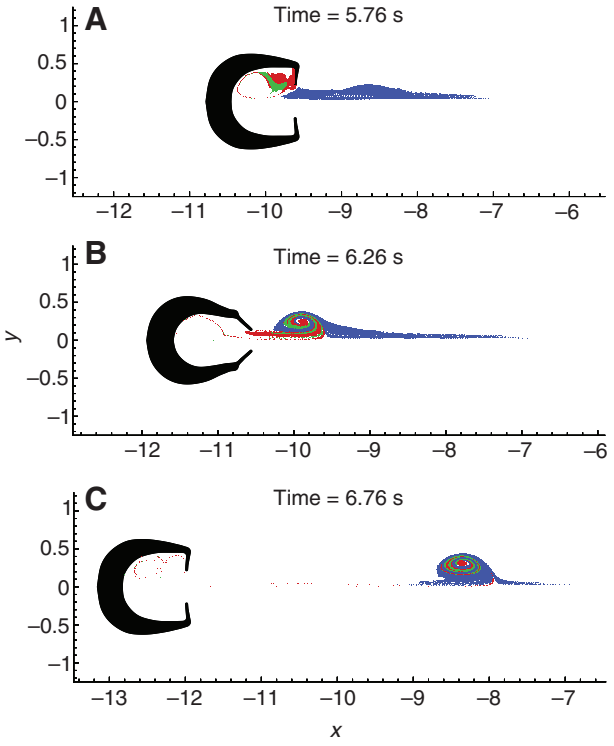

Fig. 9. Passive tracer particles for *Sarsia tubulosa*. There are three groups of tracer particles, colored green, blue and red, which are ejected as part of the same vortex. See Movie 1 in supplementary material.

Aequorea victoria

The paddling propulsion of *A. victoria* is very different from the jetting propulsion of *S. tubulosa*. This paddling or rowing propulsion produces two vortices during each swimming cycle, which are ejected together during the contraction phase. This results in more energy-efficient swimming but cannot provide the fast accelerations and rapid swimming seen in jetting hydromedusa. The LCS produced by *A. victoria* are markedly different as well. The forward and backward LCS can be seen in Fig. 10 (also see Movie 3 in supplementary material).

The *A. victoria* hydromedusa used in our simulations has a maximum bell radius of 2.3 cm and a minimum bell radius of 1.9 cm

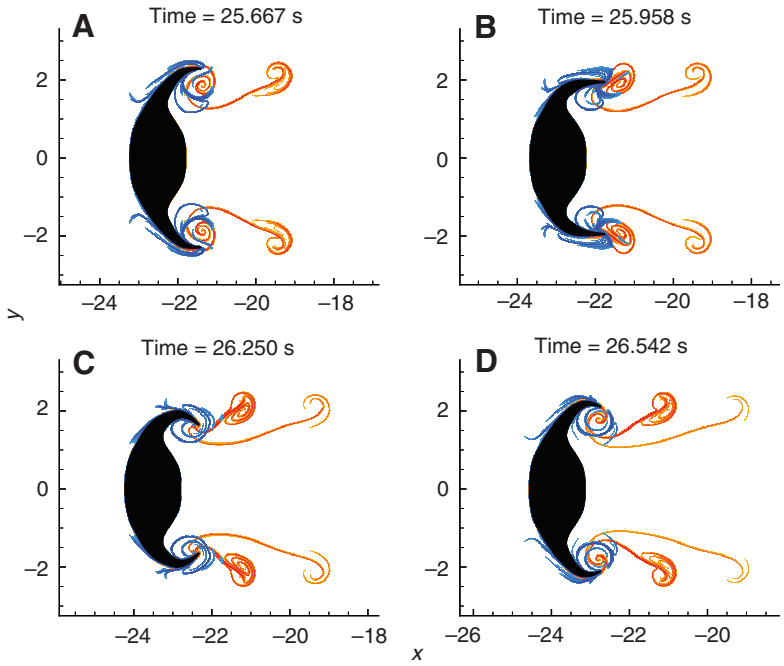

Fig. 10. Lagrangian coherent structures (LCS) for one swimming cycle of *Aequorea victoria*. The forward LCS are shown in blue and the backward LCS are red. See Movie 3 in supplementary material.

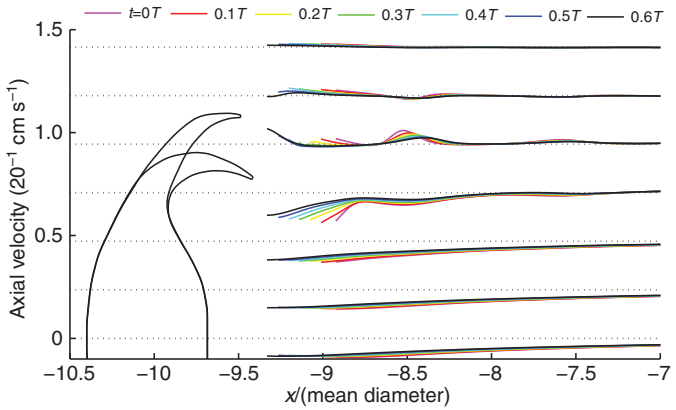

Fig. 11. The axial velocity along lines of constant radius in the wake of *Aequorea victoria*. The radius has been scaled by the mean diameter and the velocity has been scaled by a factor of 20^{-1} to fit within the figure. Many times are plotted from t=0T to t=0.8T, where T is one swimming cycle (1.17 s). For reference, the hydromedusa geometry at maximum and minimum diameter are also plotted.

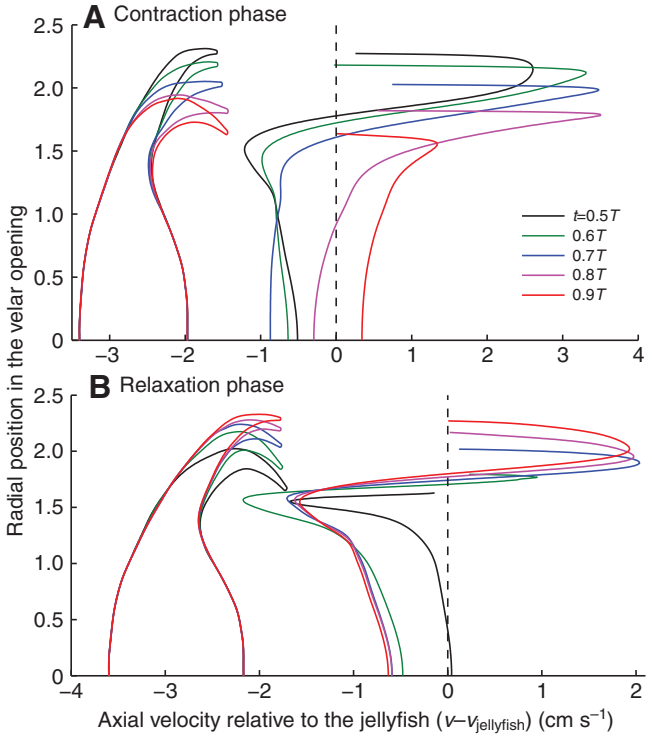

Fig. 12. The axial velocity of the flow relative to the hydromedusa across the velar opening of *Aequorea victoria*. Times are presented for one complete paddling cycle.

during contraction and is therefore much larger than *S. tubulosa*. The swimming cycle took 1.17 s, and 100 time steps per cycle were used for the CFD runs. Since *A. victoria* does not use a jetting motion to swim, the concept of a vortex formation time does not make much sense. However, if we naively define a vortex formation time by considering the volume in the subumbrellar region, this results in a formation number of $T^*\approx0.07$. A very small formation time is characteristic of a thin vortex ring located away from the axis of symmetry, which is precisely what we see in *A. victoria*. Clearly, *A. victoria* has not optimized its swimming to produce the most powerful vortices since even nozzles of constant diameter are capable of producing vortices with $T^*\approx4$ (Gharib et al., 1998).

The axial velocity in the wake is plotted in Fig. 11. Near the axis of symmetry, the flow moves toward the jellyfish, but near the bell margins the axial flow velocity oscillates with the swimming strokes. Beyond the bell margins, the flow disturbances quickly decay, leaving the flow far from the axis of symmetry largely undisturbed as well. The axial velocity across the velar opening and the pressure on the subumbrellar surface of the hydromedusa are also presented in Fig. 12 and Fig. 13. Note that, again, the large changes in velocity across the velar opening as well as pressure on the hydromedusa occur near the bell margins. Additionally, the swimming cycle for *A. victoria* is equally split into a contraction phase and a relaxation phase as it uses a rowing motion to propel itself forward.

These results are all significantly different from those seen for *S. tubulosa*, which produced velocity disturbances only near the axis of symmetry and displayed a very uniform pressure profile and velocity across the velar opening. Additionally, there is no coasting phase for *A. victoria*. Each swimming cycle is a continuous transition from contraction to relaxation and back to contraction. Due to these fundamental differences in locomotion, it is not possible to calculate the power output of *A. victoria* in the same way we have done for *S. tubulosa*. Although this is still possible, it requires a more complicated analysis of the surrounding flow.

The resulting forward and backward LCS are shown in Fig. 10. The backward LCS show attracting material manifolds and reveal vortical structures that look very similar to the results of previous dye visualization experiments (Dabiri et al., 2007; Costello et al., 2008). As discussed by Dabiri et al., the paddling type of hydromedusa creates two vortices of opposite rotation during each swimming cycle (Dabiri et al., 2007). During the relaxation phase (Fig. 10D), a stopping vortex forms in the subumbrellar region with a rotation that draws fluid towards the hydromedusa along the axis. Then, during the contraction phase (Fig. 10B), a starting vortex of opposite sense is formed very near the first, and these two vortices are ejected from the hydromedusa together. Once the vortices have been ejected, the weaker stopping vortex acts to cancel out some of the vorticity from the starting vortex. This improves the swimming efficiency of the hydromedusa (Dabiri et al., 2007). This swimming motion is repeated periodically, generating a series of vortices and propelling the hydromedusa forward. Unlike *S. tubulosa*, where only the starting vortex has been previously noted, both of these have been observed before and are known to play a key role in the swimming of *A. victoria*.

Fig. 14 and Fig. 15 show the motion of passive tracers placed in the flow that end up in the ejected vortices (also see Movie 4 in supplementary material). Note that, in Fig. 10B, during the contraction phase, the forward LCS have formed a loop along the outer surface of the bell, which is labeled A in the figure, as well as a loop in the subumbrellar region (labeled B). Tracers that end up in lobe A begin upstream of the hydromedusa in one coherent group and are swept around the tip of the bell in one cycle (see Fig. 14F to Fig. 15B). On the other hand, the tracers in lobe B are more dispersed until they group together in Fig. 14E. As a contraction takes place, lobe A is swept into the subumbrellar region, along with the tracers contained therein, and combines with lobe B, merging the two groups of tracers. From here, the tracers are immediately ejected with the next vortex pair.

Since particles (such as food) are collected at the core of the vortex, the ejected vortices and the particles contained therein remain

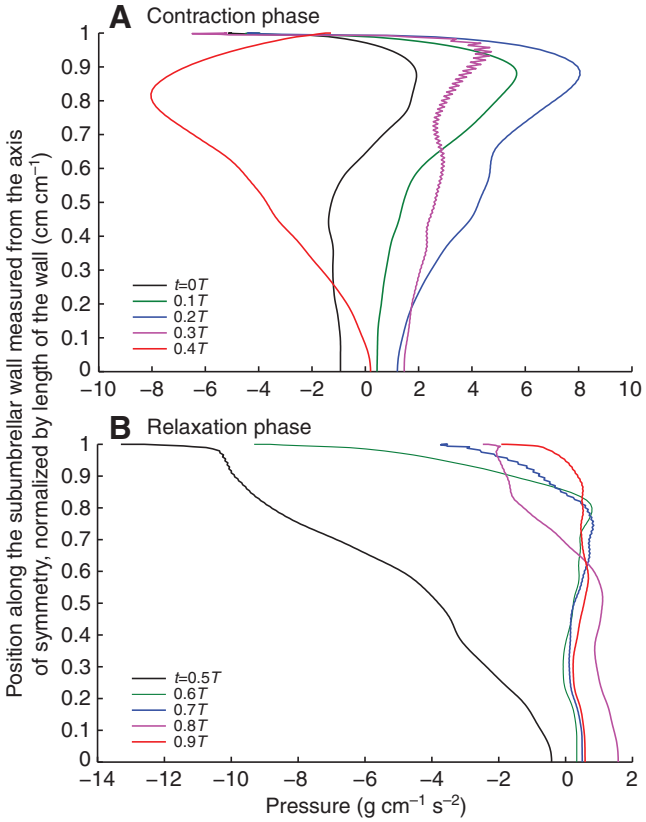

Fig. 13. The pressure on the subumbrellar wall of *Aequorea victoria* for one swimming cycle. The position is normalized by the length of the subumbrellar wall and pressure is given in g cm^{-1} s^{-2}.

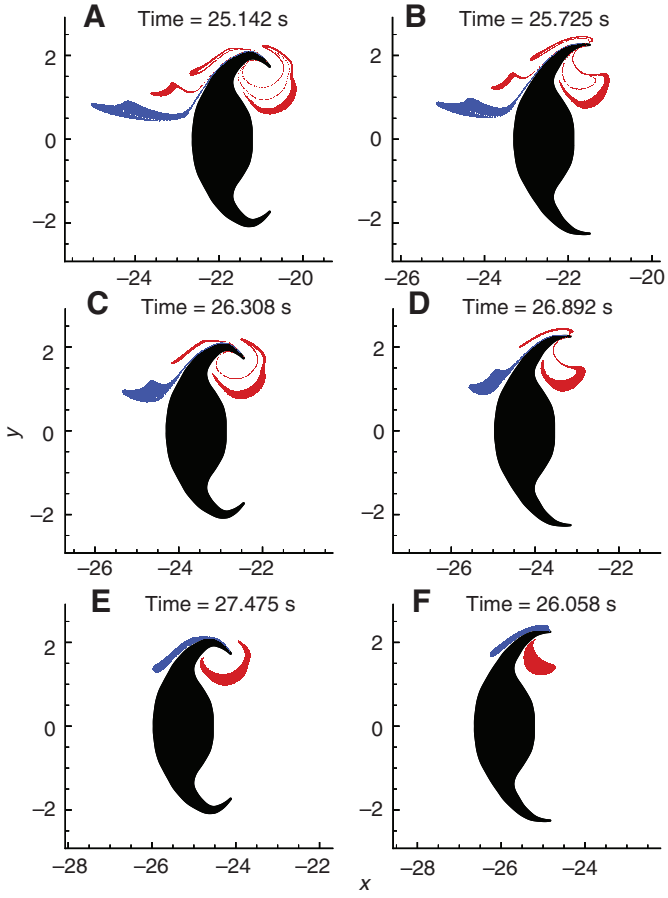

Fig. 14. Passive tracer particles for *Aequorea victoria*. There are two groups of tracer particles, colored blue and red, which are ejected as part of the same vortex. See Movie 4 in supplementary material.

at about the same radius as the bell margin and the hydromedusa's tentacles as the hydromedusa moves upstream. In fact, *A. victoria* swims with $St \approx 1.1$, meaning that the particles in a vortex separate downstream from the hydromedusa at a rate of only 1.1 radius per swimming cycle, in contrast to the 10 radius separation seen for *S. tubulosa*. This provides an excellent opportunity for the hydromedusa to feed and offers a plausible explanation for why *A. victoria* swims with its tentacles extended.

DISCUSSION

We have seen that *S. tubulosa* and *A. victoria* fall into two different categories based on their method of swimming and that feeding and swimming are coupled activities. For hydromedusae, effective feeding is completely dependent on bringing prey into contact with the tentacles or oral arms, where it may be captured. These two groups have addressed this problem in very different ways.

The jetting hydromedusa, *S. tubulosa*, retracts its tentacles while swimming and feeds primarily by ambushing its prey. Swimming is used primarily to escape predators or relocate to a new feeding location. To this end, jetting hydromedusae have optimized their swimming to move quickly, despite the extra energy costs.

Sarsia tubulosa takes advantage of its jetting motion to produce large accelerations to escape predators and reposition itself for feeding. *Aequorea victoria*, however, experiences much lower accelerations and uses swimming as an extension of its feeding mechanism. In fact, the velocity profile in the wake of *A. victoria* (Fig. 11) shows significant negative velocities in the wake near the axis of symmetry. This indicates a large added mass force that inhibits acceleration of the hydromedusa.

Aequeria victoria feeds by swimming with its tentacles extended. In fact, oblate hydromedusae spend almost all their time swimming with tentacles extended (Colin et al., 2003). This is effective because each swimming stroke acts to transport fluid that may contain food into the region of the tentacles in a way that enables prey capture (see Fig. 15C).

The relatively high Strouhal number seen for *A. Victoria* ($St \approx 1.1$) indicates that the produced vortices separate at a rate of about 1.1 hydromedusa radii per swimming cycle (see Fig. 10). During this time, the particles entrained in the vortices are transported through the tentacles, presenting an excellent opportunity for prey capture. Furthermore, as the starting and stopping vortices interact, the vortices are stretched (see Fig. 15D) and partially cancel each other due to viscous effects and vorticity diffusion, decreasing the rotation rate. This creates a relatively slowly rotating and translating vortex, further enhancing the chance for prey capture.

Sarsia tubulosa swims with a much lower Strouhal number ($St \approx 0.10$) than *A. victoria*. This means that the produced vortices move about 10 radii away from the jetting hydromedusa during each swimming cycle. This rapid transport of fluid away from the hydromedusa's body offers little opportunity for prey capture during swimming since any prey in the surrounding flow is quickly transported out of range of the tentacles.

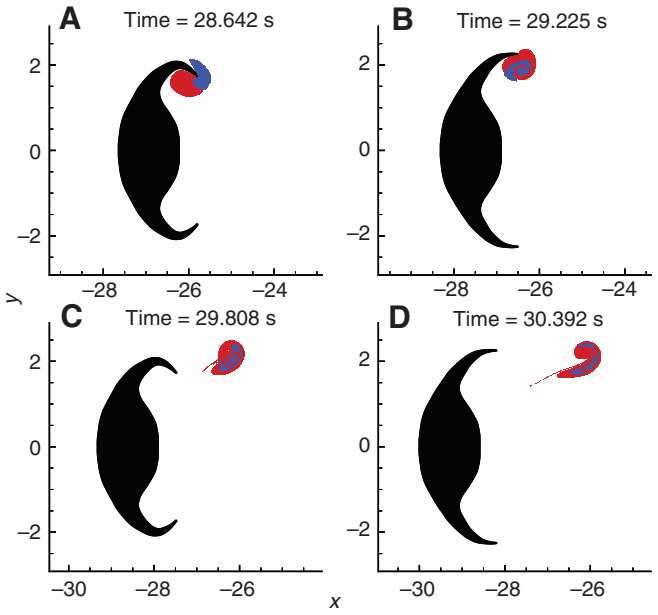

Fig. 15. Passive tracer particles for *Aequorea victoria*. There are two groups of tracer particles, colored blue and red, which are ejected as part of the same vortex. See Movie 4 in supplementary material.

Aequorea victoria primarily feed on small, soft-bodied zooplankton (Costello and Colin, 2002), which, to a good approximation, may be expected to largely drift along with the surrounding flow. Haller and Sapsis have recently examined transport of inertial particles in a general flow (Haller and Sapsis, 2008) and Peng and Dabiri have recently completed a study of the transport of inertial particles in the flow around an oblate hydromedusa, *Aurelia aurita*, using particle LCS (Peng and Dabiri, 2008) and they find regions of transport that are very similar to those seen for passive tracers. Furthermore, inertial and finite size effects decrease with prey size. If the fluid inside lobes A and B seen in Fig. 10B contains potential prey, at least a large portion of the prey will be drawn through *A. victoria*'s tentacles during swimming. In particular, lobe A is responsible for most of the transport from the upstream region into the subumbrellar region and past the tentacles. Peng and Dabiri found that 64–91% (depending on the parameters used) of the volume of capture regions for passive tracers (analogous to lobe A) was still a capture region for inertial particles (Peng and Dabiri, 2008).

The wake structures produced by these two hydromedusae also help to explain some additional features of the anatomy of oblate and prolate hydromedusae. Oblate hydromedusae commonly have well-developed and prominent oral arms extending from the center of the bell while these structures are absent in prolate species (Costello et al., 2008). In fact, the presence of well-developed oral arms or tentacles extended in the flow in a jetting species could add drag and decrease swimming performance. Conversely, paddling hydromedusae take advantage of feeding structures, such as tentacles and oral arms, drifting freely in the flow by feeding while swimming.

By using a numerical model as the basis of our study, we can easily gain additional information that would be difficult or impossible to get from experiments. For example, for *S. tubulosa*, the velocity across the velar opening is nearly uniform in space, exhibiting only a small shear layer near the velum (Fig. 4). This indicates that the fluid expelled by the hydromedusa can be well approximated as a slug of uniform velocity, perhaps with a correction for the boundary layer effects. Also, *A. victoria* swims by continuously paddling with equal times dedicated to contraction and relaxation while *S. tubulosa* follows a rapid contraction and relaxation with a brief period of coasting before the next contraction. For *S. tubulosa*, the pressure seen on the interior of the bell is also extremely uniform. This is very useful for building

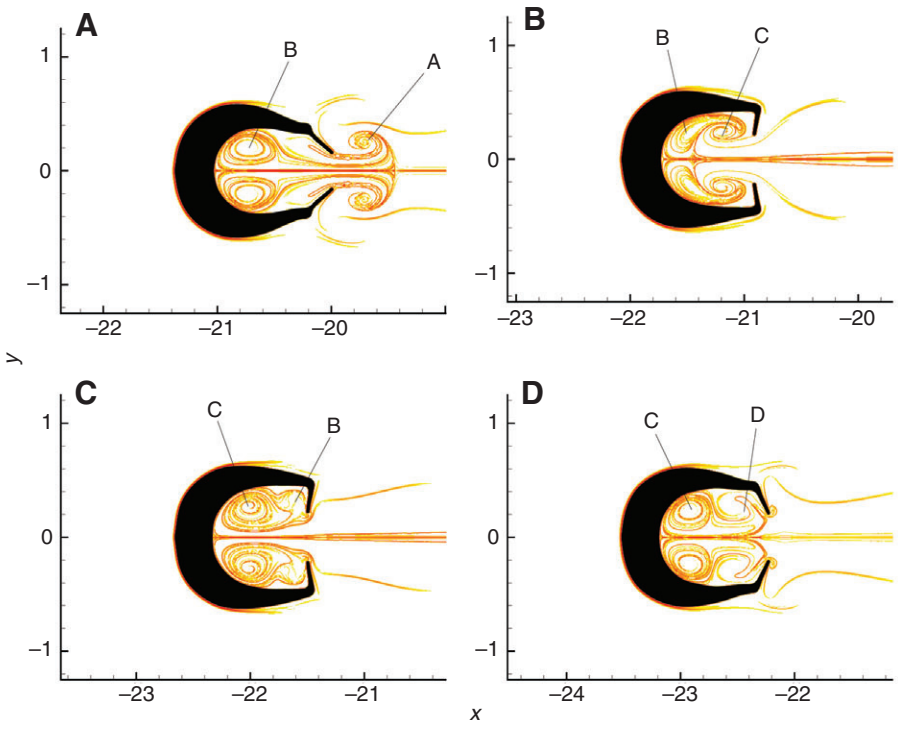

Fig. 16. Backward Lagrangian coherent structures (LCS) for *Sarsia tubulosa* showing the development of the stopping vortex. During contraction (A) starting vortex A is being ejected while stopping vortex B from the previous relaxation sits deep in the subumbrellar cavity. During relaxation (B), a new stopping vortex, C, is formed as fluid is drawn into the subumbrellar region, and stopping vortex C pushes the weaker stopping vortex B out of the way, along the walls of the cavity. In C, vortex C has settled deep within the subumbrellar cavity and vortex B has been pushed to the area near the velar opening. Vortex B is no longer recognizable as a well-defined vortex. Finally, in D, a new contraction begins. Vortex C is deep within the subumbrellar cavity while fluid in the area of vortex D, including the remnants of vortex B, will be ejected with the next starting vortex.

engineered systems to imitate the propulsion of a jetting type of hydromedusa. For example, knowing the pressure on the bell interior, combined with the velar opening diameter, would allow for the design of a piston-cylinder arrangement to mimic this behavior using current technologies. Experimental studies have little hope of obtaining these types of information due to the difficulty of directly measuring pressure on the surface of a living organism as well as the challenges of obtaining a high-resolution velocity profile.

It is important to note that these advantages do not come at the expense of relevance to biological experiments. For example, using a very simple calculation, we find that *S. tubulosa* produces a power output of about $0.33\,\mathrm{W\,kg^{-5/3}}$, which matches very well with experimental results presented by Daniel (Daniel, 1985). Additionally, even small details of the hydromedusan swimming are well captured by our method. As briefly mentioned by Daniel (Daniel, 1985), the hydromedusa is an elastic, viscously damped system. During contraction, muscles decrease the subumbrellar volume, but there are no muscles to re-expand the bell. Elastic strain energy stored during the contraction expands the bell during the relaxation phase to its resting state. Due to this elastic expansion, during the coasting phase of swimming for *S. tubulosa*, we are able to observe oscillations in both the oral cavity volume and the velar opening diameter (see Fig. 2). We attribute these oscillations to elastic effects.

Another new and interesting feature discovered in this study is the complex structure of the fluid in the subumbrellar region of *S. tubulosa* (see Fig. 1). The subumbrellar region even contains a stopping vortex that forms during the relaxation phase of swimming. However, unlike in paddling hydromedusae, this stopping vortex remains inside the subumbrellar cavity and therefore cannot influence the development of the ejected vortex.

Fig. 16 shows the development and dissipation of the stopping vortex for *S. tubulosa*. In this figure, we display only the backward LCS so that activity in the subumbrellar cavity is clear. As starting vortex A is ejected during contraction, the previous stopping vortex, B, sits deep within the subumbrellar cavity (Fig. 16A). During relaxation, a new stopping vortex, C is formed and begins to push B along the walls of the cavity (Fig. 16B) until C resides deep within the cavity and B has been pushed near the velar opening (Fig. 16C). At this point, B is no longer recognizable as a well-defined vortex. In fact, as B is pushed along the wall, C interacts with the wall to create secondary vorticity of an opposite sense to vortex C. This secondary vorticity overwhelms vortex B so that region D in Fig. 16D actually has vorticity of opposite sense to the stopping vortex. Finally, a new contraction begins and the fluid in region D (Fig. 16D) is ejected as part of a new starting vortex.

Aequorea victoria ejects both vortices together during the contraction phase while *S. tubulosa* ejects only the starting vortex while the stopping vortex remains within the bell. The different morphologies of the two hydromedusae produce this distinction. In *A. victoria*, each vortex is formed by the shear layer being shed off the tip of the bell. However, the velum of *S. tubulosa* alters the way the vortex is formed so that the stopping vortex moves deep within the velar cavity, instead of remaining near the velar opening, so it is not ejected during contraction. This stopping vortex in *S. tubulosa* has not been observed in DPIV or dye visualization experiments, most likely due to its confinement within the bell and the difficulty of imaging this area in experiments. Its effect on energy requirements and swimming efficiency remains to be seen.

LIST OF ABBREVIATIONS

Δ	finite time deformation tensor
λ_{max}	maximum eigenvalue of Δ
ALE	arbitrary Lagrangian–Eulerian
CFD	computational fluid dynamics
D_e	diameter of nozzle
DPIV	digital particle image velocimetry
FTLE	finite time Lyapunov exponent
LCS	Lagrangian coherent structure(s)
p	pressure
P_{out}	power output
$\dot{Q}$	flow rate = $-(\mathrm{d}V/\mathrm{d}t)$
r_f	final radius
r_i	initial radius
St	Strouhal number
T	integration time
T^*	dimensionless formation time
U_e	velocity of jet
V	volume
V_c	volume of cavity (subumbrellar volume)
$\mathbf{x}$	position vector
x_f	final axial position
x_i	initial axial position

The authors would like to acknowledge support from the National Science Foundation and Air Force Office of Scientific Research. The authors would also like to thank Dr Sean P. Colin of Rogers William University for providing videos used in the CFD calculations [as described in Sahin and Mohseni (Sahin and Mohseni, 2008a; Sahin and Mohseni, 2008b), which were used in the LCS calculations here.

REFERENCES

Cardwell, B. and Mohseni, K. (2008). Vortex shedding over two-dimensional airfoil: where do the particles come from? *AIAA J.* **46**, 545-547.
Colin, S. P. and Costello, J. H. (2002). Morphology, swimming performance and propulsive mode of six co-occurring hydromedusae. *J. Exp. Biol.* **205**, 427-437.
Colin, S. P., Costello, J. H. and Klos, E. (2003). In situ swimming and feeding behavior of eight co-occurring hydromedusae. *Mar. Ecol. Prog. Ser.* **253**, 305-309.
Costello, J. H. (1992). Foraging mode and energetics of hydrozoan medusae. *Sci. Mar.* **56**, 185-191.
Costello, J. H. and Colin, S. P. (1994). Morphology, fluid motion and predation by the scyphomedusae *Aurelia aurita*. *Mar. Biol.* **121**, 327-334.
Costello, J. H. and Colin, S. P. (1995). Flow and feeding by swimming scyphomedusae. *Mar. Biol.* **124**, 399-406.
Costello, J. H. and Colin, S. P. (2002). Prey resource use by coexistent hydromedusae from Friday Harbor, Washington. *Limnol. Oceanogr.* **47**, 934-942.
Costello, J. H., Colin, S. P. and Dabiri, J. O. (2008). Medusan morphospace: phylogenetic constrains, biomechanical solutions, and ecological consequences. *Invertebr. Biol.* **127**, 265-290.
Dabiri, J. O. and Gharib, M. (2005). Starting flow through nozzles with temporally variable exit diameter. *J. Fluid Mech.* **511**, 311-331.
Dabiri, J. O., Colin, S. P. and Costello, J. H. (2006). Fast swimming hydromedusae exploit velar kinematics to form an optimal vortex wake. *J. Exp. Biol.* **209**, 2025-2033.
Dabiri, J. O., Colin, S. P. and Costello, J. H. (2007). Morphological diversity of medusan lineages constrained by animal-fluid interactions. *J. Exp. Biol.* **210**, 1868-1873.
Daniel, T. L. (1983). Mechanics and energetics of medusan jet propulsion. *Can. J. Zool.* **61**, 1406-1420.
Daniel, T. L. (1985). Cost of locomotion: unsteady medusan swimming. *J. Exp. Biol.* **119**, 149-164.
Dwight, R. (2006). Robust mesh deformation using the linear elasticity equations. In *Computational Fluid Dynamics* (ed. H. Deconinck and E. Dick). New York: Springer.
Ford, M. D. and Costello, J. H. (1997). Swimming and feeding by the scyphomedusa *Chrysaora quinquecirrha*. *Mar. Biol.* **129**, 355-362.
Gharib, M., Rambod, E. and Shariff, K. (1998). A universal time scale for vortex ring formation. *J. Fluid Mech.* **360**, 121-140.
Haller, G. and Yuan, G. (2000). Lagrangian coherent structures and mixing in two-dimensional turbulence. *Physica D* **147**, 352-370.
Haller, G. and Sapsis, T. (2008). Where do inertial particles go in fluid flows? *Physica D* **237**, 573-583.
Hirt, C. W., Amsden, A. A. and Cook, J. L. (1974). An arbitrary Lagrangian-Eulerian computing method for all flow speeds. *J. Comput. Phys.* **14**, 227-253.
Johnson, A. and Tezduyar, T. (1994). Mesh update strategies in parallel finite element computations of flow problems with moving boundaries and interfaces. *Comput. Methods Appl. Mech. Engrg.* **119**, 73-94.
Krieg, M. and Mohseni, K. (2008). Thrust characterization of a bio-inspired vortex ring generator for locomotion of underwater robots. *IEEE J. Oceanic Eng.* **33**, 123-132.
Krueger, P. and Gharib, M. (2003). The significance of vortex ring formation to the impulse and thrust of a starting jet. *Phys. Fluids* **15**, 1271-1281.
Lekien, F., Coulliette, C., Mariano, A. J., Ryan, E. H., Shay, L. K., Haller, G. and Marsden, J. (2005). Pollution release tied to invariant manifolds: a case study for the coast of Florida. *Physica D* **210**, 1-20.

Lipinski, D., Cardwell, B. and Mohseni, K. (2008). A Lagrangian analysis of a two-dimensional airfoil with vortex shedding. *J. Phys. A Math. Theor.* **41**, 344011.
Madin, L. P. (1988). Feeding behavior of tentaculate predators: in situ observations and a conceptual model. *Bull. Mar. Sci.* **43**, 413-429.
Manikandan, M., Haller, G., Peacock, T., Ruppert-Felsot, J. E. and Swinney, H. L. (2007). Uncovering the Lagrangian skeleton of turbulence. *Phys. Rev. Lett.* **98**, 144502.
Mohseni, K. (2000). A: universality in vortex formation, B: evaluation of mach wave radiation in a supersonic jet. Ph.D. Thesis, California Institute of Technology, Pasadena, CA.
Mohseni, K. (2004). Pulsatile jets for unmanned underwater maneuvering. *AIAA paper 2004-6386*, Chicago, IL. 3rd AIAA Unmanned Unlimited Technical Conference, Workshop and Exhibit.
Mohseni, K. (2006). Pulsatile vortex generators for low-speed maneuvering of small underwater vehicles. *Ocean Eng.* **33**, 2209-2223.
Mohseni, K., Ran, H. and Colonius, T. (2001). Numerical experiments on vortex ring formation. *J. Fluid Mech.* **430**, 267-282.
O'Dor, R. K. (1988). Limitations on locomotor performance in squid. *J. Appl. Physiol.* **64**, 128-134.
Peng, J. and Dabiri, J. O. (2008). Transport of inertial particles by Lagrangian Coherent Structures: application to predator-prey interaction in jellyfish feeding. *J, Fluid Mech.* **623**, 75-84.
Piegl, L. (1991). On NURBS: a survey. *IEEE Comput. Graph. Appl.* **11**, 55-77.
Rom-Kedar, V. and Wiggins, S. (1990). Transport in two-dimensional maps. *Arch. Ration. Mech. Anal.* **109**, 239-298.
Saad, Y. and Schultz, M. H. (1986). Gmres: a generalized minimal residual algorithm for solving nonsymmetric linear systems. *SIAM J. Sci. Stat. Comput.* **7**, 856-869.
Sahin, M. and Mohseni, K. (2008a). An arbitrary Lagrangian-Eulerian formulation for the numerical simulation of flow patterns generated by the hydromedusa *Aequorea victoria*. *J. Comp. Phys.* **228**, 4588-4605.
Sahin, M. and Mohseni, K. (2008b). The numerical simulation of flow patterns generated by the hydromedusa *Aequorea victoria* using an arbitrary Lagrangian-Eulerian formulation. *AIAA paper 2008-3715*, University of Colorado. 38th Fluid Dynamics Conference and Exhibit.
Sahin, M., Mohseni, K. and Colin, S. P. (2009). The numerical comparison of flow patterns and propulsive performances for the hydromedusae *Sarsia tubulosa* and *Aequorea victoria*. *J. Exp. Biol.* (in press).
Shadden, S. C., Lekien, F. and Marsden, J. E. (2005). Definition and properties of Lagrangian coherent structures from finite-time Lyapunov exponents in two-dimensional aperiodic flows. *Physica D* **212**, 271-304.
Shadden, S. C., Dabiri, J. O. and Marsden, J. E. (2006). Lagrangian analysis of fluid transport in empirical vortex ring flows. *Phys. Fluids* **18**, 047105-047111.
Weston, J., Colin, S. P., Costello, J. H. and Abbott, E. (2009). Changing form and function during development in rowing hydromedusae. *Mar. Ecol. Prog. Ser.* **374**, 127-134.